

Identification of Material Parameters of PVC Foams using Digital Image Correlation and the Virtual Fields Method

P. Wang · F. Pierron · O.T. Thomsen

Received: 13 August 2012 / Accepted: 10 December 2012 / Published online: 29 December 2012
© Society for Experimental Mechanics 2012

Abstract This paper presents an effective methodology to characterize all the constitutive (elastic) parameters of an orthotropic polymeric foam material (Divinycell H100) in one single test using Digital Image Correlation (DIC) in combination with the Virtual Fields Method (VFM). A modified Arcan fixture is used to induce various loading conditions ranging from pure shear or axial loading in tension or compression to bidirectional loading. A numerical optimization study was performed with different loading angles of the Arcan test fixture and off-axis angles of the principal material axes. The objective is to identify the configuration that gives the minimum sensitivity to noise and missing data on the specimen edges, which are the two major issues when identifying the stiffness components from actual DIC measurements. Two optimized Arcan test configurations were chosen. The experimental results obtained for these two optimized test configurations show a significant improvement of the measurement accuracy compared with a pure shear load configuration. The larger sensitivity of the pure shear test to missing data as opposed to the tensile test is also evident from the experimental data and confirms the analysis from the optimization study. The recovery of missing data along the specimen edges is a promising way to further improve the identification results.

Keywords Full-field measurements · Digital image correlation · Virtual fields method · Polymeric foam

Introduction

Lightweight sandwich structures are being increasingly used for a variety of applications including wind turbine blades, marine and aerospace structures, and applications for general transportation purposes. The core materials used in such sandwich structures are commonly polymer closed cell foams, such as e.g. PVC, PMI or PET foams. Ideally, polymer foam core materials are considered as homogenous isotropic materials. However, in practice most polymer foams display both heterogeneous and anisotropic material behaviour due to the density variations and directionality of foam cells developed during the manufacturing process. Therefore accurate experimental characterization of the mechanical behaviour of polymeric foam materials is essential for their efficient use in sandwich structures, as well as for the development of accurate numerical models on the material and structural levels. The mechanical behavior of polymeric foams for simple stress states including uniaxial tension, compression and shear has been studied extensively in the literature [1–4]. However, to identify all elastic stiffness parameters, these studies rely on the use of several tests including uniaxial tension, compression and shear, along with point-wise or area-wise deformation measurement instrumentation like extensometers or strain gauges. More recent work by Zhang et al. [5] and Taher et al. [6] characterized the H100 Divinycell PVC foam using Digital Image Correlation (DIC). The results of these two studies show a good agreement with the datasheet from the manufacturer [7], and it is further demonstrated that the use of the DIC technique makes it possible to eliminate the influence of parasitic effects due to the stiffness difference between the

P. Wang (✉) · O.T. Thomsen
Department of Mechanical and Manufacturing Engineering,
Aalborg University, Aalborg, Denmark
e-mail: pwa@m-tech.aau.dk

F. Pierron
Châlons-en-Champagne campus, Arts et Métiers ParisTech,
Châlons-en-Champagne, France

F. Pierron · O.T. Thomsen
School of Engineering Sciences, University of Southampton,
Southampton, UK

extensometer and the foam. However, a significant amount of time and effort was spent on designing the different test specimen shapes needed to reach a uniform stress/strain state in the gauge area. To circumvent this problem, different methodologies have been proposed to solve the inverse problem, which is defined as the identification of a set of constitutive material parameters from the measurement of kinematic quantities (displacements, strains, etc.), some load information and the knowledge of the geometry and boundary conditions. Among these inverse approaches can be mentioned the finite element model updating technique [8], the constitutive equation gap method [9], and the Virtual Fields Method (VFM) [10].

The Virtual Fields Method is an effective test technique to characterize the material properties directly from full-field measurements. This method takes advantage of the heterogeneous strain fields obtained through full-field measurement techniques, such as Digital Image Correlation (DIC) [11], speckle pattern interferometry [12] or grid methods [13], for instance, and uses only one single test to identify all the material constitutive parameters. The effectiveness of the method is underlined by the fact that it does not require the use of iterative direct problem solutions to solve the inverse problem. Thus, the VFM approach is much less time consuming than e.g. classical finite element model updating approaches, and the VFM associated with full-field deformation measurements is becoming widely used for the extraction of constitutive parameters for composites and other types of materials. However, there have been relatively few studies concerning polymer foam materials using this technique. As an illustration, the first attempt at identifying Poisson's ratios of standard low-density (homogeneous) polyurethane foams by using DIC and VFM was only published recently [14].

One of the most important issues in such inverse procedures is to choose a suitable test configuration. Since the heterogeneous stress/strain fields play an important role in the identification procedure, it is very important to have a test configuration that activates all the sought constitutive parameters of the materials under investigation (i.e., the actual stress/strain fields must be sufficiently sensitive to variations of each of the sought parameters). Optimization of the test configuration for VFM identification was firstly proposed by Pierron et al. (2007) [15]. The idea was to find an optimized specimen length and a material orthotropic axis angle so as to minimize a cost function based on the sensitivity to noise of the sought material stiffness components. Recently, a refined test configuration design procedure was proposed by Rossi and Pierron [16]. The study used the grid method as the full-field technique and simulated the whole measurement and identification chain, including image forming and grid method algorithm. This study provided a significant improvement of the optimization procedure by

introducing the many different types of error sources into the cost function. However, this approach was not fully validated experimentally. Moreover, it used a specific test fixture, namely the unnotched Iosipescu test as in [15], and it is important to extend the optimization to other test configurations and full-field techniques, like DIC. Also more experimental work needs to be done to validate the optimization study.

This paper presents a methodology developed to identify all the orthotropic elastic parameters of polymer foams in one single test using Digital Image Correlation in combination with the Virtual Fields Method. A modified Arcan fixture [6, 17] was used to provide loading in different directions. The loading angle and the off-axis angle of the material principal direction are used as the two design variables. Noise and missing data effects are introduced as the two main error sources to construct the cost function to optimize the test configuration. After deciding on the optimized test configurations, experimental validation was undertaken on both optimized and poor test configurations. The results are compared with the reference parameters obtained using the conventional uniaxial testing procedures.

Test Setup

Test Specimen and Modified Arcan Fixture

The material studied in this paper is the closed-cell cross-linked Divinycell H100 PVC foam manufactured by DIAB [7]. All specimens in this study were prepared from one 60 mm panel. It has been shown [5] that this material has orthotropic/transversely isotropic properties due to the different lengths of the foam cells in the rising (through-thickness) and in-plane directions, respectively, generated in the manufacturing process. This can also be observed from microscopic images [5]. Therefore the material principal axes are defined as the above two directions. A modified Arcan fixture was used to characterize the constitutive parameters of the foam. This fixture has been developed recently to identify orthotropic material parameters [6, 17]. It has an S-shape composed of two arms (shown in Fig. 1). By connecting different loading holes on the arms, more complex loading conditions can be introduced compared with the conventional Arcan fixture. Besides the different combinations of shear and tensile loads, the modified Arcan fixture can also introduce compression loading. A previous study using this modified Arcan fixture provided very reliable test results for a PVC foam material [6, 17]. However, since the PVC foam is orthotropic, the use of multiple tests to obtain the stiffness parameters is time consuming, as both through-thickness and in-plane specimens have to be prepared. Furthermore, different specimen shapes are needed to

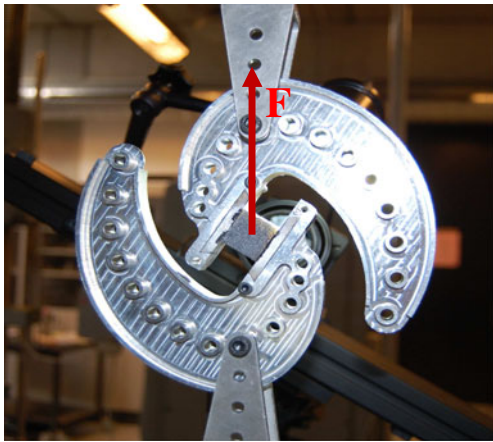


Fig. 1 Modified Arcan fixture with multiaxial loading

ensure a well defined stress/strain state in the gauge area of the shear, tension and compression test specimens.

In this study there is no need to attempt to obtain homogeneous stress/strain fields, since DIC combined with the Virtual Fields Method allows for the identification of constitutive parameters from heterogeneous strain fields. On the contrary, heterogeneity is required for the simultaneous identification of all stiffness components. This is very important as it provides much more freedom to choose loading and boundary conditions as well as specimen geometry in the mechanical test. Here a small $20 \times 20 \text{ mm}^2$ rectangular block was used to induce a heterogeneous strain field dominated by shear and longitudinal tensile stresses (bending). Compressive stress concentrations occur near the ends of the bonded region. Since this material has different mechanical properties in the through-thickness (1) and in-plane (2) directions, all the orthotropic stiffness components should be involved in the full deformation maps of this test. It should be noted that there is some density variation inside the foam panel due to the manufacturing process, especially towards the top and bottom surfaces of the panel. Therefore the foam specimens with different off-axis angles θ were cut with high precision using a 3-axis CNC milling machine from the central part of a thick foam panel so as to avoid including material from the top and bottom surfaces. Material direction 1 is the through thickness direction and material direction 2 is the in plane direction. After milling, the two sides of specimens perpendicular to the x-axis were bonded to aluminium tabs using Araldite epoxy adhesive (visible in Fig. 2) and fixed into the S-shape modified Arcan fixture.

DIC Testing Setup for the Multi-axial Arcan Test

2D digital image correlation was used to capture the deformation of the foam specimens. A random grey scale pattern

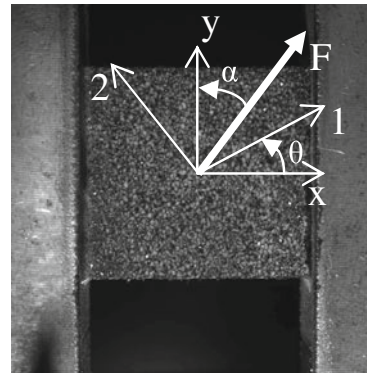
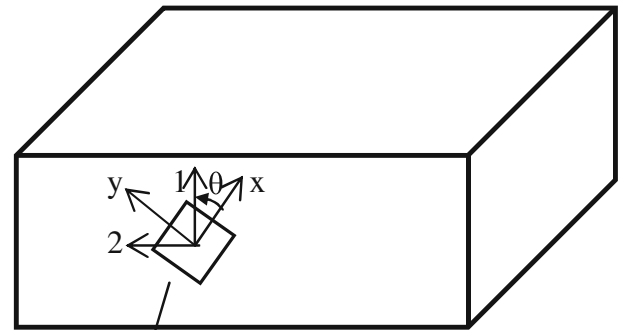


Fig. 2 Schematic of the test

was applied onto the specimen surface using spray paint. An Aramis 4 M system [18] was used to capture a series of images during deformation and to perform correlation between the deformed and undeformed images. The basic idea is to divide each image into many small computational units called facets or subsets. The displacement was computed at the centre of each facet by correlating the random speckle pattern. The strain components can then be obtained by numerical differentiation. A larger square facet includes a wider variation in grey levels and reduces the noise in the results. However, the spatial resolution is reduced when increasing the facet sizes. Here a particular set-up (Fig. 3) was used to measure the heterogeneous deformation fields on the two back-to-back specimen planes.



Fig. 3 2D DIC measurement set-up

Two cameras with a resolution of 2048×2048 pixel² each were placed on opposite sides of the specimen to capture the images on both sides simultaneously. The square shaped specimen was loaded multi-directionally using the modified Arcan fixture. The cameras were rotated according to the loading angle of the specimen so that the displacements and strains were computed along the global coordinate direction of the specimen (x and y , see Fig. 2). The advantage of this set-up is that it enables the elimination of out-of-plane movements by averaging the measured values from the two cameras. It can also account for possible through-thickness gradients of the strain field. This was already successfully employed in [19]. The detailed performance of this set-up is reported in Table 1. Resolutions were evaluated as the standard deviation of the displacement and strain maps of two consecutive images of the stationary specimen.

VFM Techniques Applied to the Multi-axial Arcan Test

The basic idea of the VFM is to express the condition of global equilibrium of the tested specimen using the principle of virtual work. The principle of virtual work without body force and in quasi-static situation can be expressed as:

$$\int_V \sigma : \varepsilon^* dV = \int_{\partial V} \bar{T} \cdot u^* dS \quad (1)$$

where ‘:’ denotes the contracted product of the stress tensor σ and the virtual strain tensor ε^* , and ‘·’ denotes the dot product between the external traction force vector \bar{T} and the virtual displacement vector u^* . The equation expresses the condition of global equilibrium between the internal virtual work over the specimen volume V and the external virtual work over the boundary surface of V . The only condition on the vectorial function u^* is that it is continuous and

Table 1 The performance report of the DIC set-up

Technique Used	Mono image correlation
Subset size	40×40 pixel ²
Shift	20 pixel
Camera	8 bit, 2048×2048 ARAMIS 4 M system
Field of view	$26 \text{ mm} \times 26 \text{ mm}$
Measurement points	5776
Displacement	
Spatial resolution	0.51 mm/40 pixel
Resolution	0.14 μm
Strain	
Smoothing method	Gaussian Average (3×3)
Differentiation method	Finite differences
Resolution	1.2×10^{-4}

differentiable over the domain V . It is then assumed that the specimen material (polymer foam) can be described as a homogeneous, orthotropic and linear elastic solid, and that the specimen is under a state of plane stress. The constitutive equation of the foam can therefore be written as (in the material orthotropy axes):

$$\begin{Bmatrix} \sigma_1 \\ \sigma_2 \\ \sigma_6 \end{Bmatrix} = \begin{bmatrix} Q_{11} & Q_{12} & 0 \\ Q_{12} & Q_{22} & 0 \\ 0 & 0 & Q_{66} \end{bmatrix} \begin{Bmatrix} \varepsilon_1 \\ \varepsilon_2 \\ \varepsilon_6 \end{Bmatrix} \quad (2)$$

where σ_i , ε_i , ($i=1,2,6$) are the in-plane stress and strain components according to the so-called contracted notation [20], and Q_{ij} ($i, j=1,2,6$) are the in-plane stiffness components. Substituting the stress components with the actual strains and constitutive parameters, equation (1) can be rewritten as:

$$\begin{aligned} & Q_{11}t \int_S \varepsilon_1 \varepsilon_1^* dS + Q_{22}t \int_S \varepsilon_2 \varepsilon_2^* dS + Q_{12}t \\ & \times \int_S (\varepsilon_1 \varepsilon_2^* + \varepsilon_2 \varepsilon_1^*) dS + Q_{66}t \\ & \times \int_S \varepsilon_6 \varepsilon_6^* dS = t \int_{L_f} (T_1 u_1^* + T_2 u_2^*) dl \end{aligned} \quad (3)$$

where t is the thickness of the specimen. Since the elastic strain fields are known from the full-field measurement, and since the resulting force applied to the specimen is known from the load cell readings, a new set of equations can be obtained in which only the elastic parameters are unknown for each new selected virtual field. When choosing at least as many independent virtual fields as unknowns, all the parameters can be identified directly by solving the resulting linear system [10].

For the construction of the virtual fields, piecewise functions were used in this study [10, 21]. This method uses shape functions $\Phi^{(i)}$ which are similar to that employed in finite element analysis. They express the virtual displacement u^* at any points in the solid as a function of the virtual displacement $u^{*(i)}$ at the nodes of a mesh as demonstrated in equation (4):

$$u^* = \sum_{i=1}^n \Phi^{(i)} u^{*(i)} \quad (4)$$

where n is the number of nodes per element. In the present study, bilinear shape functions with 4-noded quadrilateral elements have been used. The shape functions and nodal displacement in the element are defined as:

$$\Phi : \begin{bmatrix} \Phi^{(1)} & 0 & \Phi^{(2)} & 0 & \Phi^{(3)} & 0 & \Phi^{(4)} & 0 \\ 0 & \Phi^{(1)} & 0 & \Phi^{(2)} & 0 & \Phi^{(3)} & 0 & \Phi^{(4)} \end{bmatrix} \quad (5)$$

$$\mathbf{u}^{*(i)} : \begin{bmatrix} u_1^{*(1)} \\ u_2^{*(1)} \\ u_1^{*(2)} \\ u_2^{*(2)} \\ u_1^{*(3)} \\ u_2^{*(3)} \\ u_1^{*(4)} \\ u_2^{*(4)} \end{bmatrix} \quad (6)$$

The virtual strain component in the elements are obtained by differentiating equation (4)

$$\varepsilon^* = \sum_{i=1}^n S\Phi^{(i)}u^{*(i)} \quad (7)$$

where S is a linear differential operator defined as:

$$(\eta_{ij})^2 = \left(\frac{S}{n_p}\right) \left[\begin{aligned} &((Q_{11})^2 + (Q_{12})^2) \sum_{i=1}^{n_p} (\varepsilon_1^{*(ij)})^2 + ((Q_{22})^2 + (Q_{12})^2) \sum_{i=1}^{n_p} (\varepsilon_2^{*(ij)})^2 + \dots \\ &\dots + 2((Q_{11})^2 + (Q_{22})^2) \sum_{i=1}^{n_p} \varepsilon_1^{*(ij)} \varepsilon_2^{*(ij)} + (Q_{66})^2 \sum_{i=1}^{n_p} (\varepsilon_6^{*(ij)})^2 \end{aligned} \right] \quad (10)$$

where S is the measurement area, n_p is the amount of data points. By rewriting equation (10), sensitivity to noise parameters can be expressed as:

$$(\eta_{ij})^2 = \frac{1}{2} Y^{*(ij)T} H Y^{*(ij)} \quad (11)$$

where $Y^{*(ij)}$ is a vector with virtual nodal displacements. H is a square matrix which contains the unknown stiffness parameters and the formulation of the virtual strain component from equation (7). Previous work in [10] has proved that $(\eta_{ij})^2$ exhibits a unique minimum. So the minimization of $(\eta_{ij})^2$ will be a criterion to choose the virtual fields $Y^{*(ij)}$. The Lagrangian L associated with the constrained minimization problem can be written as:

$$L = \frac{1}{2} Y^{*(ij)T} H Y^{*(ij)} + \Lambda^{(ij)T} (A Y^{*(ij)} - Z^{(ij)}) \quad (12)$$

$\Lambda^{(ij)}(A Y^{*(ij)} - Z^{(ij)})$ defines the constraints of this minimization problem. The first constraint is that the virtual field must be kinematically admissible (mainly continuity conditions). The second one is that the virtual field must be special so that stiffness parameters can be obtained directly. $\Lambda^{(ij)}$ is a vector containing the Lagrange multipliers. A is the matrix of describing the constraints. $Z^{(ij)}$ is a vector containing only zeros except one component which is equal to one. The location of this nonzero component depends on which stiffness is to be

$$S : \begin{bmatrix} \frac{\partial}{\partial x} & 0 \\ 0 & \frac{\partial}{\partial y} \\ \frac{\partial}{\partial y} & \frac{\partial}{\partial x} \end{bmatrix} \quad (8)$$

As a potentially infinite number of virtual fields can be found, an additional criterion was employed to select the virtual fields optimally and automatically aiming at minimizing noise influence on the identified parameters. The detailed derivation of this procedure is proposed in the optimized VFM theory [10]. The basic idea is to assume a Gaussian white noise added to the actual strain fields. Then it is proved in [10] that the standard deviation $\sigma_{Q_{ij}}$ of each constitutive parameter Q_{ij} is directly proportional to the standard deviation γ of the strain noise:

$$\sigma_{Q_{ij}} = \gamma \eta_{ij} \quad (9)$$

where η_{ij} describes the sensitivity of each constitutive parameter to the noise in the VFM identification procedure. The expression of $(\eta_{ij})^2$ is derived as:

identified with this particular special field. Four optimized virtual fields are defined by solving this problem after changing the position of the 1 in the $Z^{(ij)}$ vector.

The minimization of Lagrangian L is obtained by solving the following linear system:

$$\begin{bmatrix} H & A^T \\ A & 0 \end{bmatrix} \begin{Bmatrix} Y^{(ij)} \\ (ij) \end{Bmatrix} = \begin{Bmatrix} 0 \\ Z^{(ij)} \end{Bmatrix} \quad (13)$$

After obtaining the virtual nodal displacement vector $Y^{*(ij)}$, the unknown stiffness parameters Q_{ij} are required to determine η_{ij} . The idea here is to give some initial value of Q_{ij} and find a first set of four special optimized virtual fields to provide updated values of Q_{ij} . Then the new Q_{ij} parameters are used in the next iteration to find the new virtual fields, etc. Previous work [10] has shown that the iterative procedure generally converges quickly within two loops regardless of the choice of initial values for the Q_{ij} .

In the present study, $4 \times 4 = 16$ virtual elements have been employed here which gives a total of 50 virtual degrees of freedom. The convergence study indicated that 4×4 element size was enough to provide stable identification and save computing time compared with a higher number of virtual elements. The area S_2 where the strains are processed by the VFM is shown in Fig. 4. It has been moved slightly away

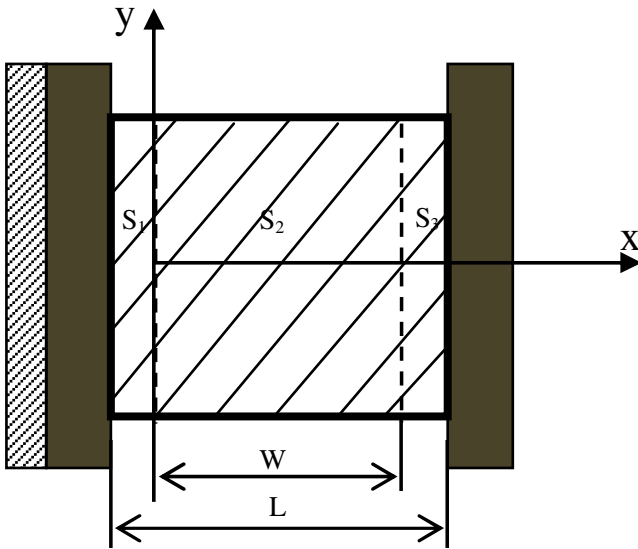


Fig. 4 Measurement area S_2 used for identification ($W/L=0.95$)

from the glued specimen boundaries because accurate data are difficult to obtain close to edges. Also, the fixture casts some shadow which makes it difficult to obtain data right to the edge. The ratio between the length W of the field of view and the specimen length L is 0.95 (see Fig. 4).

Therefore the area of the specimen is divided into three parts: one area with actual deformation fields being measured (S_2) and two areas without actual strain field measurements (S_1 and S_3). By separating the integrals in the principle of virtual work and assuming a state of plane-stress, equation (3) can be rewritten as (14):

$$-\int_{S_1} \sigma : \varepsilon^* dS - \int_{S_2} \sigma : \varepsilon^* dS - \int_{S_3} \sigma : \varepsilon^* dS + \int_{\partial S_1} \bar{T} \cdot u^* dl + \int_{\partial S_2} \bar{T} \cdot u^* dl + \int_{\partial S_3} \bar{T} \cdot u^* dl = 0 \tag{14}$$

As a consequence of the above, the virtual displacements on areas S_1 and S_3 are constrained to be rigid body-like so that missing experimental data on these two areas will not appear in the final equation (zero virtual strain fields cancelling out the virtual work of internal forces on S_1 and S_3). Therefore, the terms related to actual stress σ on areas S_1 and S_3 should be removed in equation (14). Since no external force is applied on S_2 , equation (14) becomes:

$$-\int_{S_2} \sigma : \varepsilon^* dS + \int_{\partial S_3} \bar{T} \cdot u^* dl = 0 \tag{15}$$

The virtual displacement on S_1 is selected to be zero. For S_3 , the total force F measured from the load cell can be

divided into two resultant components F_x and F_y by relation (16).

$$F_x = F \sin \alpha, F_y = F \cos \alpha \tag{16}$$

where α is the loading angle relative to the global coordinate direction (Fig. 2). Hence the virtual work of the external forces on S_3 can be written as:

$$\int_{\partial S_3} \bar{T} \cdot u^* dl = \int_{\partial S_3} \left\{ \begin{matrix} f_1(y) \\ f_2(y) \end{matrix} \right\} \left\{ \begin{matrix} u_1^* \\ u_2^* \end{matrix} \right\} dl \tag{17}$$

where f_1 and f_2 are the horizontal and vertical linear force distribution along the boundaries, respectively. Since only the resultant force F is measured and the virtual displacement has to be rigid body-like on S_3 , the horizontal and vertical virtual displacements on this area are defined as constants a and b . Therefore, equation (17) transforms into:

$$\int_{\partial S_3} \bar{T} \cdot u^* dl = \left\{ \begin{matrix} a \\ b \end{matrix} \right\} \left\{ \begin{matrix} \int_{\partial S_3} f_1(y) dy \\ \int_{\partial S_3} f_2(y) dy \end{matrix} \right\} \tag{18}$$

Since the resultant is only known in the vertical direction (direction of F in Fig. 2), a good choice for a and b is:

$$\left\{ \begin{matrix} a = \sin \alpha \\ b = \cos \alpha \end{matrix} \right. \tag{19}$$

and the virtual work of external forces reduces to F .

In addition, the continuity conditions of the virtual displacement field lead to the following constraints on the boundary of S_2 when automatically selecting piecewise optimized virtual fields:

$$\left\{ \begin{matrix} u_1^{*(S_2)}(x=0, y) = 0 \\ u_2^{*(S_2)}(x=0, y) = 0 \end{matrix} \right. \tag{20}$$

$$\left\{ \begin{matrix} u_1^{*(S_2)}(x=L, y) = a \\ u_2^{*(S_2)}(x=L, y) = b \end{matrix} \right. \tag{21}$$

Since the specimens might be cut in different off-axis angles relative to the material principal directions, the actual strain and virtual strain fields should be transferred along the material principal direction from the global coordinate system when identifying the orthotropic material parameters. The transformation relation is given in equations (22) and (23) below.

$$\left\{ \begin{matrix} \varepsilon_{11} \\ \varepsilon_{22} \\ \varepsilon_{12} \end{matrix} \right\} = \begin{bmatrix} c^2 & s^2 & 2cs \\ s^2 & c^2 & -2cs \\ -2cs & 2cs & 2(c^2 - s^2) \end{bmatrix} \left\{ \begin{matrix} \varepsilon_{xx} \\ \varepsilon_{yy} \\ \varepsilon_{xy} \end{matrix} \right\} \tag{22}$$

$$c = \cos \theta, s = \sin \theta \tag{23}$$



where θ is the off-axis angle relative to the material principal direction (Fig. 2).

Optimization Study of the Test Configuration using Simulation Data

One important feature of the VFM identification methodology is that the quality of the identification depends on the test configuration. Therefore an optimized test configuration should be sought that activates all the stress components to provide a balanced identification of all stiffness parameters. The idea is to choose several design variables that can be easily adjusted to change the test configuration. Then an optimization routine is introduced to find the best combination of the design variables that leads to the best identification results. In the modified Arcan fixture test several design variables could be considered. The measurement area, loading angle and principal material directions are obvious variables that affect the identification performance. However, to ensure that the loading axis passes through the centre point of the specimen, the distance between the two bonded edges was fixed to 20 mm. Therefore, the measurement area could only be varied freely along the unglued specimen sides (y direction). In order to utilize the pixels of the cameras optimally, a $20 \times 20 \text{ mm}^2$ specimen dimension is best because it has the same aspect ratio as that of the CCD camera (2048×2048), as shown in [16] for a similar test configuration. As a result, the design variables selected here are the loading angle and the material principal direction. The loading angle can be adjusted by connecting to different holes of the modified Arcan fixture. The change in material principal direction is obtained by cutting the specimen in different directions within the foam slab. Finite Element analyses were conducted using ANSYS version 13.0 along with the ANSYS APDL language, to create 361 simulated tests with different combinations of the two design variables. The model was built-up using the quadrilateral isoparametric element PLANE 82, with eight nodes and sixteen degrees of freedom (DOF). The 80×80 mesh density was selected by considering the numerical convergence and also approximated to the amount of experimental data points (76×76) to avoid bring any significant influence from spatial resolution difference. Here the amount of simulation data points is relatively larger than the experimental one as additional data points would be removed later for studying the missing data effect. The two arms of the Arcan fixture were simulated as rigid bodies. The material principal direction was varied from 0° to 90° with increments of 5° . The load angle was varied from 0° to 90° (pure shear to pure tension) with increments of 5° . All strain maps were input into a MATLAB VFM identification routine, which was adjusted according to the loading and material angles. During this identification process, two main

error sources were introduced. One is measurement noise, and the other is missing data at the edges. A cost function must be defined to describe the stability of the identified parameters with respect to the different error sources. The procedure results in plots of the cost function as a contour map with respect to the two design variables.

First, the effects of measurement noise were studied. Due to the effect of noise, the measured strain values are different from the exact ones which will cause some scatter on the identified stiffness parameters. In this optimization study, the sensitivity to noise parameters were used to form a cost function to find the test configuration which led to the most balanced simultaneous identification of all stiffness parameters. The chosen cost function is identical to that used in [15] for the unnotched Iosipescu test. The relative sensitivity to noise parameters r_{ij} used in the cost function are defined by the ratio of sensitivity parameter η_{ij} by the corresponding stiffness parameter Q_{ij} . Since the orders of magnitude of the different Q_{ij} are sometimes quite different, relative sensitivity parameters η_{ij}/Q_{ij} can give more clear representation of the impact of η_{ij} on the corresponding stiffness parameters. The parameter r_{12} corresponding to Q_{12} was not included in the cost function to avoid the cost function being dominated by this term which is inherently larger than the other r_{ij} parameters. The chosen cost function C_1 is:

$$C_1 = \frac{(r_{11} - r_{22})^2 + (r_{22} - r_{66})^2 + (r_{11} - r_{66})^2}{(r_{11} + r_{22} + r_{66})^2} \quad (24)$$

The contour map of this cost function is shown in Fig. 5. It can be seen that the material principal direction (also referred to as the ‘off-axis angle’) is the most important factor to obtain balanced parameter identification. When the material principal axes coincide with the specimen coordinate system, it is difficult to obtain an accurate

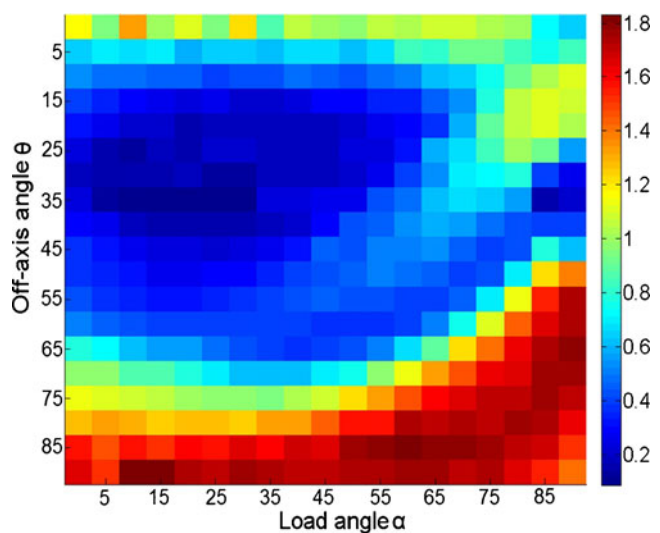


Fig. 5 Cost function for the noise sensitivity study

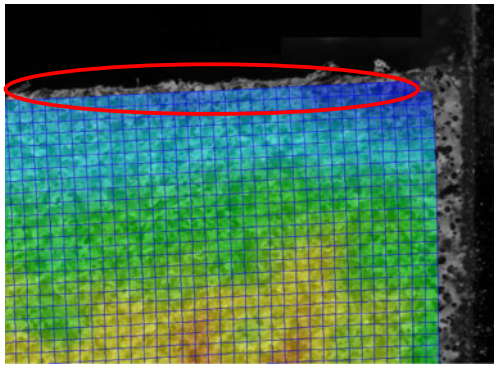


Fig. 6 The facets on the edge of the specimen

identification of all four stiffness parameters regardless of the loading direction. The test configurations with off-axis angles between 25° and 65° provide good identification with the lowest combined sensitivity to noise. Two local minima can be observed; one is located at $(\theta=35^\circ, \alpha=30^\circ)$, and the other at $(\theta=35^\circ, \alpha=85^\circ)$. Since the modified Arcan fixture vary from 0° to 90° with increments of 15° , the off-axis tensile test configuration $(\theta=35^\circ, \alpha=90^\circ)$ will be selected instead of the test configuration $(\theta=35^\circ, \alpha=85^\circ)$.

Missing Data Effect

Because of the intrinsic nature of the DIC algorithms, at least half a facet size is lost at the edges of the field of view (as shown Fig. 6). Reducing the facet size is a way of addressing this issue but unfortunately, this also increases the noise level.

This issue is not important on the right and left hand side edges as the VFM identification area can be easily adjusted in the horizontal direction, as shown above. However, if data are missing at the top and bottom edges, this means that the fraction of the shear/tension force going through this section will be missing in the equilibrium equation, resulting in significant overestimation of the stiffnesses.

This was already demonstrated in [16]. In practice, at least one row of data points at the edges is normally incomplete and has to be deleted before inputting the strain maps into the virtual fields routine. In the current study, the effect of missing data at the top and bottom specimen edges has been investigated by removing two rows of data points on each edges of the specimen (5 % of total cross section data points) in the simulated strain maps. Two rows of data were also removed from the right and left hand side edges, but this did not lead to a VFM artifact. The relative error of each of the identified stiffness parameters is computed as:

$$E_{rel}(Q_{ij}) = \frac{|Q_{ij} - Q_{ijref}|}{Q_{ijref}} \quad (25)$$

where Q_{ij} is the stiffness parameter identified from VFM routine and Q_{ijref} is the reference stiffness input into the FE model. The results shown in Fig. 7 indicate that missing data on the upper and bottom free edges bring significant bias on the identified material parameters. The main reason is the formulation of virtual fields method. In Fig. 3, the specimen was separated into 3 areas and different virtual fields were defined in these 3 areas to take into account that no strain data was available on S_1 and S_3 . Since the virtual displacement on

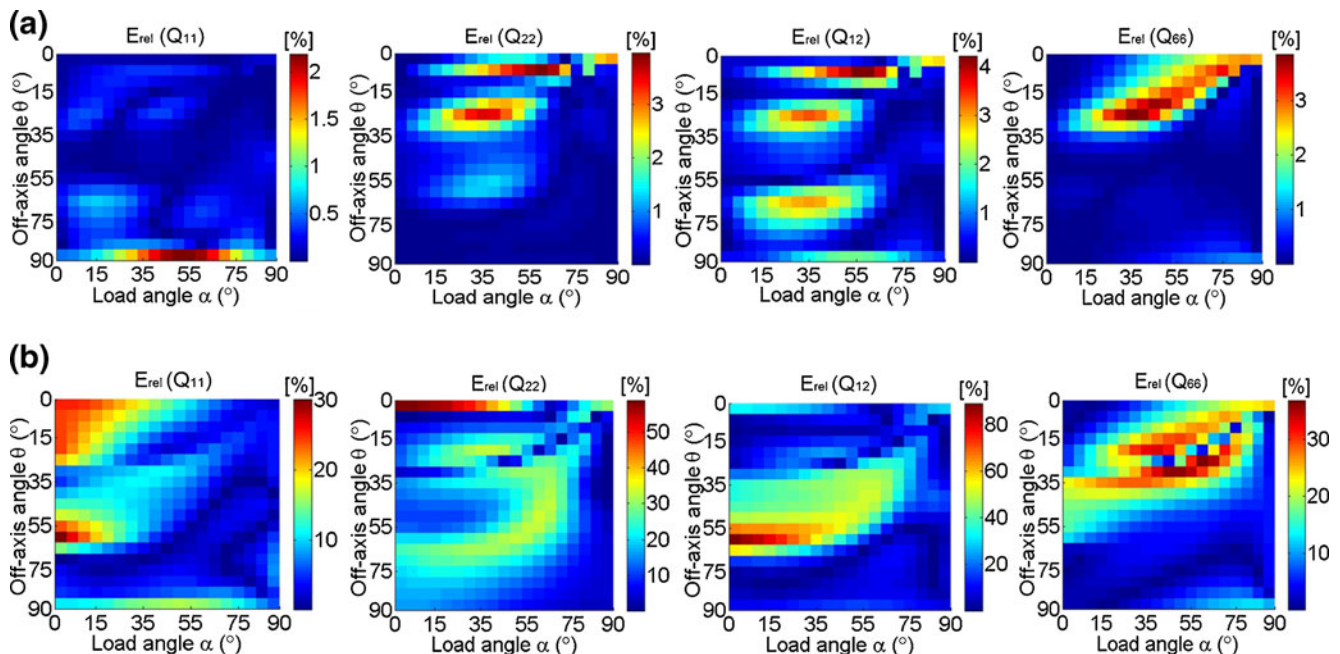


Fig. 7 (a) Relative error of each of the identified parameters with missing data on the *left and right sides* (b) Relative error of each of the identified parameters with missing data on the *upper and bottom edges*

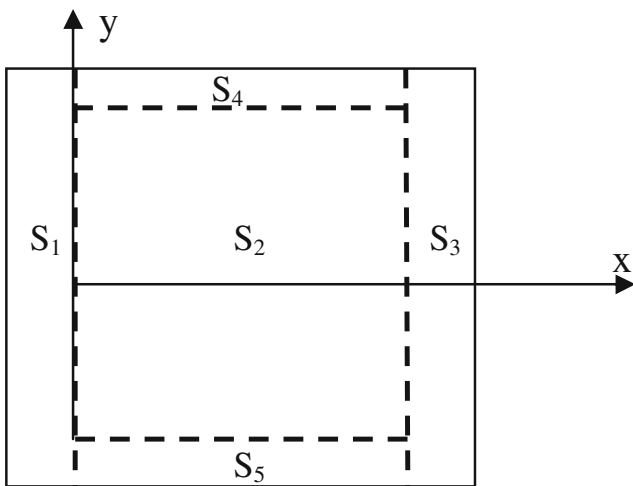


Fig. 8 The measurement area S_2 used for identification with missing data on free edges

S_1 and S_3 are set to be rigid body, the principle of virtual work is written as in equation (15). However due to the missing data on the free edges, the actual strains are also not available in the areas S_4 and S_5 shown in Fig. 8. Thus, equation (15) can be rewritten as:

$$\begin{aligned}
 & - \int_{S_2} \sigma : \varepsilon^* dS - \int_{S_4} \sigma : \varepsilon^* dS - \int_{S_5} \sigma : \varepsilon^* dS + \int_{\partial S_3} \bar{T} \cdot u^* dl \\
 & = 0
 \end{aligned}
 \tag{26}$$

where $\int_{S_4} \sigma : \varepsilon^* dS$ and $\int_{S_5} \sigma : \varepsilon^* dS$ are the error terms introduced by the missing data effect. It could be possible to assign rigid body-like virtual fields to S_4 and S_5 as well but the

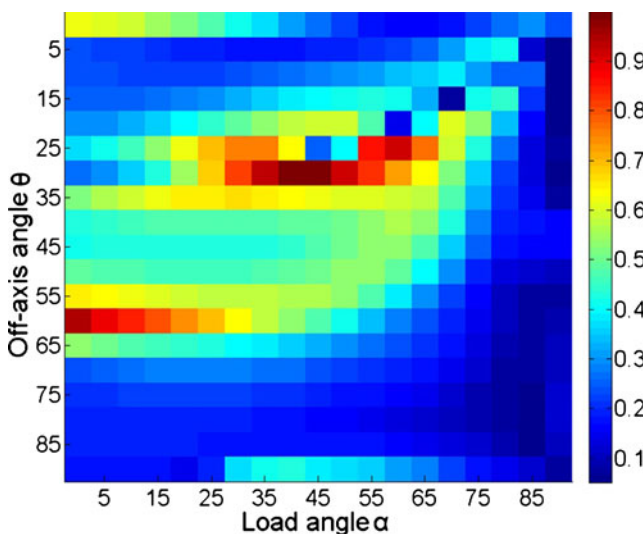


Fig. 9 The cost function for missing data sensitivity study (missing 5 % of total datas)

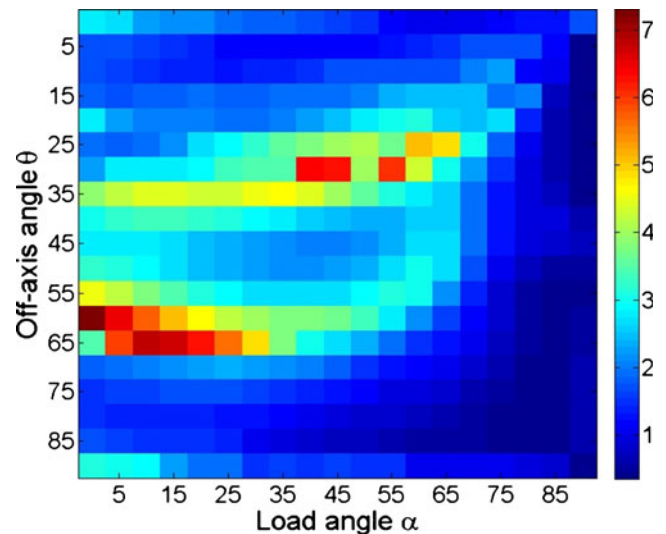


Fig. 10 The cost function for missing data sensitivity study (missing 20 % of total datas)

continuity conditions on the virtual displacements would then result in the impossibility to involve the applied force in the equation. In this case, only stiffness ratios could be identified, not actual stiffness values

A new cost function C_2 was defined to find the optimized test configuration with minimal influence of the missing data effect. This cost function represents the overall variation before and after accounting for missing data on the free edges, and is given in equation (27).

$$C_2 = \sqrt{\left(\frac{Q_{11}-Q_{11ref}}{Q_{11ref}}\right)^2 + \left(\frac{Q_{22}-Q_{22ref}}{Q_{22ref}}\right)^2 + \left(\frac{Q_{12}-Q_{12ref}}{Q_{12ref}}\right)^2 + \left(\frac{Q_{66}-Q_{66ref}}{Q_{66ref}}\right)^2}
 \tag{27}$$

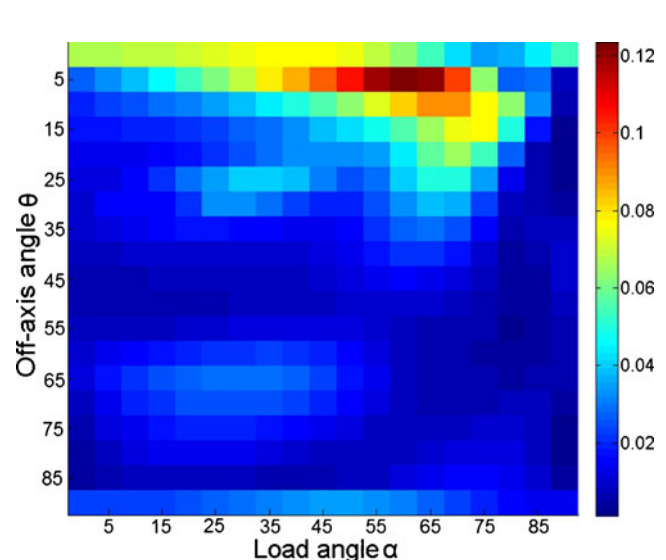
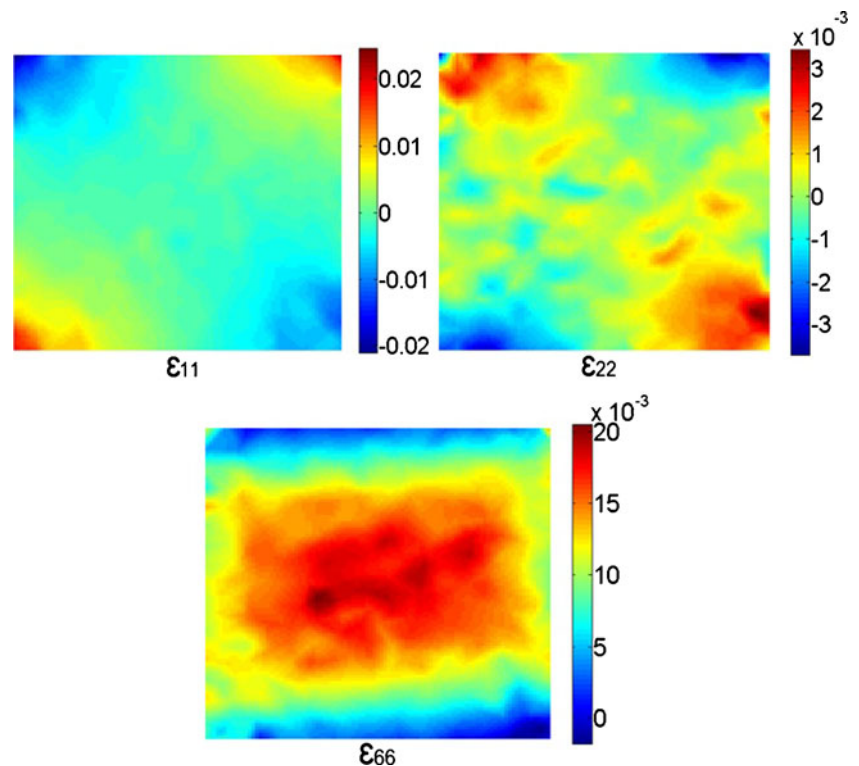


Fig. 11 Cost function with extrapolation of missing data

Fig. 12 DIC strain maps for the $\theta=90^\circ$ and $\alpha=0^\circ$ test configuration (*pure shearing*)



In equation (27) Q_{ijref} are the reference values of the four identified material stiffness parameters, and Q_{ij} are the identified parameters affected by missing data. The plot of this cost function contour map is shown in Fig. 9. The results indicate that the loading angle becomes the main issue affecting the sensitivity of the identified parameters to the missing data effect. For some shear and biaxial loading test configuration, the overall identification error of four stiffness parameters becomes extremely significant. The best area in this map is close to a loading angle equal to 90° which corresponds to the tensile test configuration. This can be explained by realizing that when the test configuration is close to a pure shear test of the foam block ($\theta=0$), a bending moment is effectively induced

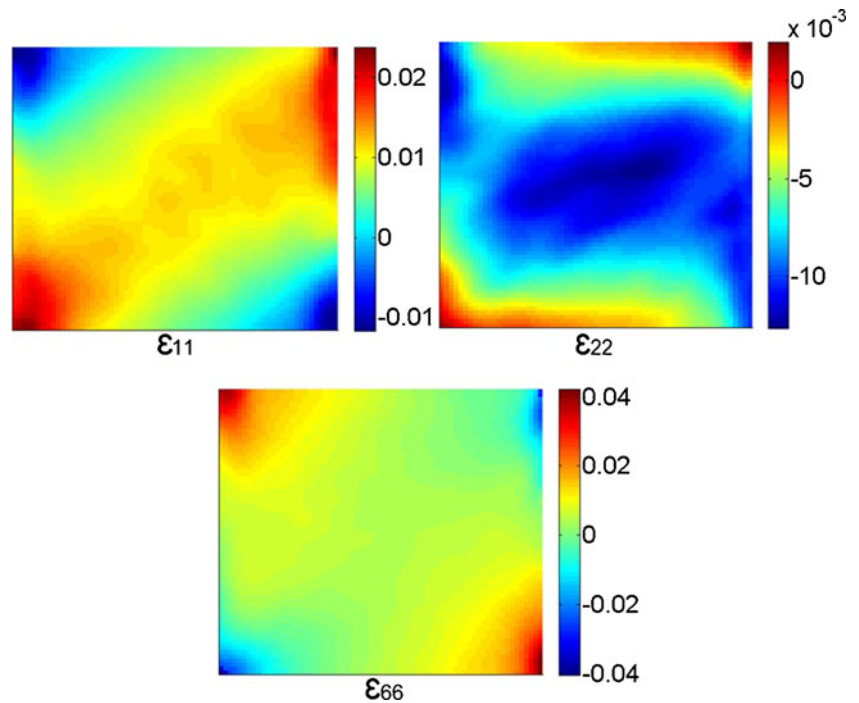
which produces large bending stresses at the free edges, resulting in a more significant error on the equilibrium equation when data points are missing there.

Combining this result with the conclusion from the noise sensitivity study, it is found that the best test configuration to minimize the noise effect in Fig. 5 is around $\theta=35^\circ$ and $\alpha=30^\circ$, while the best configuration to minimize the missing data effect is around $\theta=35^\circ$ and $\alpha=90^\circ$. Therefore it is important to make a compromise between these two factors in the actual test. It can be noted that there are some singularities at several locations in Fig. 9 ($\theta=25^\circ$ and $\alpha=45^\circ$, etc.). The main reason is that some ‘bad’ test configurations are very sensitive to the missing data effect. So the results produced by these ‘bad’ test configurations are very

Table 2 $\theta=90^\circ$ and $\alpha=0^\circ$ pure shear test configuration

MPa	After extrapolation				Before extrapolation			
	Q_{11}	Q_{22}	Q_{12}	Q_{66}	Q_{11}	Q_{22}	Q_{12}	Q_{66}
Test1	20.3	73.4	4.15	28.7	59.5	83.5	19.0	29.0
Test2	1.06	66.0	0.01	30.6	12.9	78.0	2.33	32.5
Test3	13.0	71.3	2.35	32.1	43.0	80.9	11.1	34.9
Test4	3.44	70.0	0.670	32.0	20.7	80.2	6.06	33.4
Average	9.45	70.2	1.80	30.9	34.0	80.6	9.63	32.5
Ref(AAU) [6]	140	63.5	23.6	32.5	140	63.5	23.6	32.5
Ref(SOU) [5]	143	63.4	26.0	30.1	143	63.4	26.0	30.1
Relative Difference	93.3 %	10.6 %	92.4 %	1.28 %	75.7 %	26.9 %	59.2 %	3.83 %

Fig. 13 DIC strain maps for the $\theta=35^\circ$ and $\alpha=30^\circ$ test configuration (*multi axial loading*)



unstable and easily affected by the amount of missing data. The experimental study in the next section also indicates that these ‘bad’ test configurations are very sensitive to virtual mesh sizes. Therefore, the optimized test configuration is selected by looking for the spots with lowest value of cost function and also the area around these spots. Figure 10 shows the cost function contour created by increasing the amount of missing data. The overall identification error for the four stiffness parameters increases a lot compared with the results in Fig. 9 but the number of ‘singular points’ is greatly reduced, even though they tend to happen in the same location of the design space. Although there is a slight variation between the patterns of the two cost function, the best areas (around tensile loading angle) of these two contours are still very stable and consistent.

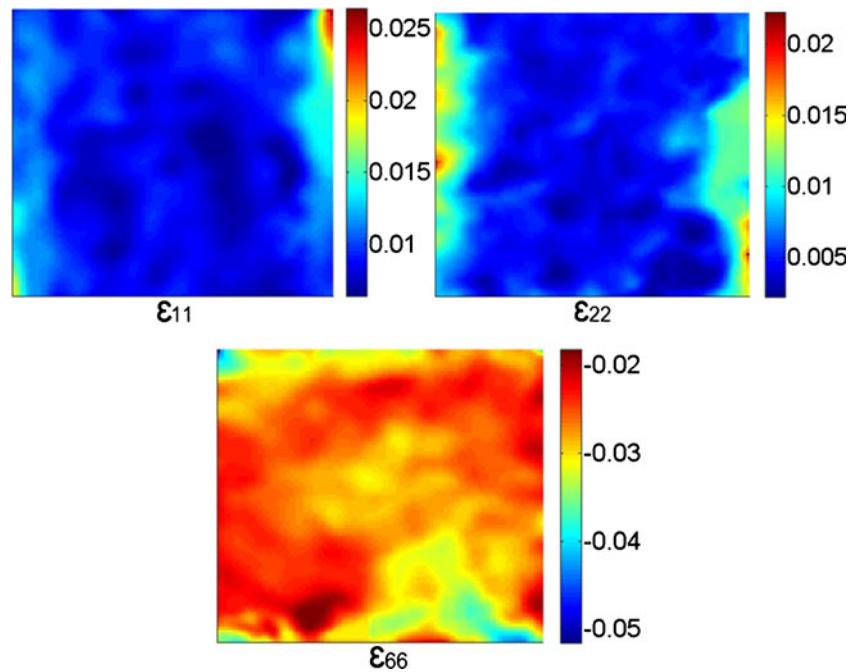
Recovery of Missing Data

Since the missing data effect has a large influence on the present procedure, it is considered to reduce its impact by extrapolating the 2D data (strain) maps to reconstruct the missing data points at the two free edges. The idea is to use the nearest data points and to copy them to the missing data positions (‘padding’ procedure). The cost function contour map after conducting this extrapolation is shown in Fig. 11. The maximum value is around 0.12, which is much smaller than the value shown in Fig. 9. This indicates that a much better parameter identification can be achieved when the missing data have been recovered. The plot in Fig. 11 also indicates that the poor test configurations represented by the central part of the cost function map shown in Fig. 9

Table 3 $\theta=35^\circ$ and $\alpha=30^\circ$ multi-axial test configuration

MPa	After extrapolation				Before extrapolation			
	Q ₁₁	Q ₂₂	Q ₁₂	Q ₆₆	Q ₁₁	Q ₂₂	Q ₁₂	Q ₆₆
Test1	156	73.9	11.1	35.5	165	101	19.8	46.3
Test2	152	77.3	9.98	34.6	159	94.2	14.7	43.6
Test3	158	81.0	11.3	34.0	170	101	19.3	45.9
Test4	148	69.2	8.05	33.6	158	88.6	13.2	40.6
Average	154	75.4	10.1	34.4	163	96.2	16.7	44.1
Ref(AAU)[6]	140	63.5	23.6	32.5	140	63.5	23.6	32.5
Ref(SOU)[5]	143	63.4	26.0	30.1	143	63.4	26.0	30.1
Relative Difference	8.83 %	18.8 %	59.2 %	9.90 %	15.2 %	51.5 %	32.7 %	40.9 %

Fig. 14 DIC strain maps for the $\theta=35^\circ$ and $\alpha=90^\circ$ test configuration (*off-axis tensile*)



experienced significant improvement when missing data recovery was performed. Nevertheless, choosing a test configuration which can give less sensitivity to missing data is still important even with the extrapolation of 2D data maps. By combining the plots in Figs. 5, 9 and 11 it is found that $\theta=35^\circ$ and $\alpha=90^\circ$ provides the best compromise. Therefore this configuration has been selected for the experimental validation. Another good test configuration is the biaxial loading test with $\theta=35^\circ$ and $\alpha=30^\circ$. The reason that this test configuration was also selected for the experimental validation is that it has the minimal cost function value when only noise is considered (see Fig. 5). Thus, if the error from missing data can be reduced to a very low level, this test configuration should provide the best parameter identification. A comparison of the two configurations discussed above will provide insight into the real practical effect of missing data.

Experimental Validation and Discussion

This section presents the experimental results aiming at validating the above findings from the numerical test optimization study. The two optimized test configurations selected from above have been used. The pure shear test configuration ($\theta=90^\circ$, $\alpha=0^\circ$) was also chosen for comparison. First, the pure shear test was performed. Reference values for the elastic properties were obtained using ASTM standard tests in [5], as well as from measurements conducted using the modified Arcan fixture with tensile tests along the in-plane and through-thickness directions and shearing tests using butterfly-shaped specimens [6]. The strain maps for the pure shear test are given in the material orthotropy axes in Fig. 12. The load is applied up to around 150N with 5 load steps. Previous work [6] gave the tensile and shear stress vs. strain curves until failure, which

Table 4 $\theta=35^\circ$ and $\alpha=90^\circ$ off-axis tensile test configuration

MPa	After extrapolation				Before extrapolation			
	Q ₁₁	Q ₂₂	Q ₁₂	Q ₆₆	Q ₁₁	Q ₂₂	Q ₁₂	Q ₆₆
Test1	144	75.4	19.4	29.5	147	77.3	20.9	30.6
Test2	152	78.8	19.0	31.6	157	84.2	19.7	33.6
Test3	148	78.0	20.1	31.3	150	81.1	21.3	31.9
Test4	150	71.2	18.0	28.2	153	74.6	18.2	30.6
Average	148	75.9	19.1	30.2	152	79.3	20.0	31.7
Ref(AAU)[6]	140	63.5	23.6	32.5	140	63.5	23.6	32.5
Ref(SOU)[5]	143	63.4	26.0	30.1	143	63.4	26.0	30.1
Relative Difference	4.59 %	19.5 %	23.0 %	3.51 %	7.42 %	25.0 %	19.4 %	1.28 %

Table 5 $\theta=35^\circ$ and $\alpha=30^\circ$ multi-axial test configuration with different virtual mesh sizes

MPa	Mesh 4×4	Mesh 6×6	Mesh 10×10	Ref(AAU)	Ref(SOU)
Q_{11}	156	155	150	141	143
Q_{22}	73.9	50.8	35.7	63.5	63.4
Q_{12}	11.1	6.61	3.02	23.6	26.0
Q_{66}	35.5	29.7	21.4	32.5	30.1

indicates that the linear elastic region extends up to around 4 % elastic tensile strain. Hence the strain maps selected here are derived within the linear elastic region. The identified parameters for the 4 specimens are listed in Table 2. The relative difference is given by comparing the average testing results and the mean value of two sets of reference data. It can be seen from the results that the most reliably determined parameters in the present pure shear loading test configuration are Q_{22} and Q_{66} , which is due to the predominant longitudinal bending and shear stresses/strains in the specimen. It is problematic to attempt extracting Q_{11} and Q_{12} from this (pure shear) test configuration because of the very low levels of transverse stress. Thus, Q_{11} and Q_{12} exhibit a large bias even when applying the extrapolation on the edges of the data maps.

The strain maps obtained for the ($\theta=35^\circ$ and $\alpha=30^\circ$) test are shown in Fig. 13, and the identification results are listed in Table 3. Compared with the results in Table 2, the identified parameters are all much closer to the reference values. There is some difference, however, relative to the reference values. This is especially the case for the stiffness Q_{22} , which is nearly 51 % larger than the reference value. When correcting for missing data points at the upper and lower edges, a significant improvement is obtained wrt. identification of the parameters Q_{11} , Q_{22} and Q_{66} . This is especially the case for Q_{22} . However, there is still a large bias on Q_{12} , which in any case is the most difficult parameter to identify. The only parameter which is slightly less accurately determined than in the pure shear test is Q_{66} . This was expected because some shear modulus sensitivity was sacrificed to get more balanced values for the other stiffness components. The fact that the missing data correction has a large effect on the identified values is consistent with the results of Fig. 9 for this particular test configuration.

The final test configuration is the off-axis tensile test ($\theta=35^\circ$ and $\alpha=90^\circ$). Comparing the strain maps of this test (Fig. 14) with the results of the other tests (cf. Fig. 12 and

Fig. 13), it is observed that the two optimized positions gave much more balanced strain values for all components with non zero values over most of the field of view, whereas in the shear test, most of the significant normal strain values are concentrated at the corners. The identification results are reported in Table 4. For the results without any data extrapolation on the edges to recover missing data, the off-axis tensile test gives much more accurate results than those listed in Table 3. Thus, the correction for missing data brings the results slightly closer to the reference values, but at the same time the variation is much smaller than for the results of the other tests. This is again consistent with the findings reported in Fig. 9. The most stable parameter identified in the current test is Q_{66} . This was expected since off-axis tensile tests induce very large shear strains, and such test configuration is therefore commonly used to determine the in-plane shear modulus of anisotropic materials [22]. The major limitation of the standard off-axis tensile test is that it is very hard to produce a homogeneous stress/strain distribution in the specimen gauge section. However by using DIC and VFM this problem is solved. Finally, the reason why this test configuration leads to the best results is apparent when comparing Fig. 14 with Fig. 13. The off-axis tensile test provides much less spatial heterogeneity. As a consequence, the limited spatial resolution of DIC has less impact on the strain maps for this test than for the biaxial one. This could certainly be seen if the procedure presented in [16] was used here to simulate the speckle deformation. This is one of the improvements that will be sought in the future.

To further evaluate the two optimized test configurations, different virtual element mesh sizes were used to extract the stiffness parameters from the DIC strain data. Table 5 and Table 6 show the comparison between the two test configurations using different virtual mesh sizes. It is observed that the results of the off-axis tensile tests are much more stable than those obtained from the off-axis multi-axial shear test,

Table 6 $\theta=35^\circ$ and $\alpha=90^\circ$ off-axis tensile test configuration with different virtual mesh sizes

MPa	Mesh 4×4	Mesh 6×6	Mesh 10×10	Ref(AAU)	Ref(SOU)
Q_{11}	144	138	136	141	143
Q_{22}	75.4	66.5	58.7	63.5	63.4
Q_{12}	19.4	27.8	31.6	23.6	26.0
Q_{66}	29.5	29.9	30.2	32.5	30.1

especially for the identification of the parameters Q_{22} , Q_{12} and Q_{66} . Again, this is certainly caused by the more pronounced strain heterogeneities which are not well tackled by the DIC measurements. Although the off-axis tensile test gives a relatively reliable identification, there are still some differences between the identified parameters and the reference values. However, significant density variations exist within the tested PVC foam panels [5], and this may account for some of the differences observed. However, the important variations observed for Q_{22} and Q_{12} when the virtual mesh size is varied indicate that there are some unresolved issues in the present methodology. In particular, the effect of smoothing, speckle quality etc. is yet to be evaluated. Thus, as already suggested above, the next step is to set up a complete identification simulation based on the procedure proposed in [16] to track all possible sources of bias, and based on this to choose regularizing parameters (subset size, smoothing...) in a more rational way.

Conclusions and Future Work

In this study, the simultaneous identification of the orthotropic stiffness components of a PVC foam was undertaken using Digital Image Correlation and the Virtual Fields Method. A modified Arcan test fixture was used, and an optimization routine was developed to identify the best test configuration as a function of loading angle and material principal directions. The effect of noise and missing data were included into the optimization study as the two main error sources. The experimental results validated the optimization study.

The main conclusions are summarized as follows:

1. The experimental results validated the finding of the numerical optimization study in that the off-axis tensile test gave an improved identification of the orthotropic stiffness components of the PVC foam.
2. Missing strain data at the free edges proved to have a very significant influence on the identification results. This was accounted for by using a data extrapolation scheme which proved to be successful.
3. The larger sensitivity of the shear test to missing data as opposed to the off-axis tensile test was also revealed in the experimental data and confirmed the numerical analysis results. This is due to large bending stresses at the free edges of the specimen.
4. The identification results were significantly affected by the size of the virtual mesh, particularly for the parameters Q_{22} and Q_{12} . This may be caused by errors introduced by inappropriate spatial resolution of the measurements. Different virtual fields process the bias caused by inappropriate local spatial resolution differently, hence different stiffness values are obtained. The only way to assess this issue rigorously is to simulate the DIC measurements. To do so, a procedure like that in [16] will be set up in the near future to bring further improvements to the current procedure.
5. Finally, when the procedure is ready, it can be used to evaluate the variation of properties within a slab by testing many of these small specimens cut at different locations within the slab. This should provide an invaluable insight into the mechanical variability of the foam.

Acknowledgments The research reported was sponsored by the Danish National Advanced Technology Foundation through the project “Advanced Thermal Breaker”, which is carried out in close collaboration with Fiberline Composites A/S. The financial support is gratefully acknowledged.

References

1. Gdoutos EE, Daniel IM, Wang KA (2001) Multiaxial characterization and modeling of a PVC cellular foam. *J Thermoplast Compos Mater* 14(5):365–373
2. Kanny K, Mahfuz H, Thomas T, Jeelani S (2004) Static and dynamic characterization of polymer foams under shear loads. *J Compos Mater* 38(8):629–639
3. Kabir ME, Saha MC, Jeelani S (2006) Tensile and fracture behavior of polymer foams. *Mater Sci Eng, A* 429(1–2):225–235
4. Daniel I, Cho JM (2011) Characterization of Anisotropic Polymeric Foam under Static and Dynamic Loading. *Exp Mech* 51(8):1395–1403
5. Zhang S, Dulieu-Barton JM, Fruehmann R, Thomsen OT (2012) A methodology for obtaining material properties of polymeric foam at elevated temperatures. *Exp Mech* 52(1):3–15
6. Taher ST, Thomsen OT, Dulieu-Barton JM, Zhang S (2011) Determination of mechanical properties of PVC foam using a modified Arcan fixture. *Compos Appl Sci Manuf* 43(10):1698–1708
7. DIAB (2011) Divinycell PVC datasheet. <http://www.diabgroup.com>
8. Geymonat G, Hild F, Pagano S (2002) Identification of elastic parameters by displacement field measurement. *CR Mecanique* 330(6):403–408
9. Claire D, Hild F, Roux S (2002) Identification of damage fields using kinematic measurements. *CR Mecanique* 330(11):729–734
10. Pierron F, Grédiac M (2012) *The Virtual Fields Method*. Springer New York. ISBN 978-1-4614-1823-8
11. Chu TC, Ranson WF, Sutton MA, Peters WH (1985) Applications of digital image correlation techniques to experimental mechanics. *Exp Mech* 25(3):232–244
12. Bruno L, Poggialini A (2005) Elastic characterization of anisotropic materials by speckle interferometry. *Exp Mech* 45(3):205–212
13. Surrel Y (1994) Moiré and grid methods: a signal processing approach. *Proc SPIE* 2342:213–220
14. Pierron F (2010) Identification of Poisson’s ratios of standard and auxetic low density polymeric foams from full-field measurements. *J Strain Anal Eng Des* 45(4):233–25
15. Pierron F, Vert G, Burguete R, Avril S, Rotinat R, Wisnom M (2007) Identification of the orthotropic elastic stiffnesses of composites with the virtual fields method: sensitivity study and experimental validation doi:10.1111/j.1475-1305.2007.00346.x. *Strain* 43(3):250–25
16. Rossi M, Pierron F (2012) On the use of simulated experiments in designing tests for material characterization from full-field measurements. *Int J Solids Struct* 49(3–4):420–435
17. Taher ST, Thomsen OT, Dulieu-Barton JM (2011) Bidirectional thermo-mechanical properties of foam core materials using DIC. *Thermomech Infrared Imaging* 7:67–7418

18. ARAMIS user manual, GOM. <http://www.gom.com>
19. Moulart R, Avril S, Pierron F (2006) Identification of the through-thickness rigidities of a thick laminated composite tube. *Compos Appl Sci Manuf* 37(2):326–336
20. Robert MJ (1998) *Mechanics Of Composite Materials*. CRC Press. ISBN-10: 156032712X.
21. Toussaint E, Grédiac M, Pierron F (2006) The virtual fields method with piecewise virtual fields *Int J Mech Sci* 48(3):256–264. doi:10.1016/j.ijmecsci.2005.10.002
22. Pierron F, Vautrin A (1994) Accurate comparative determination of the in-plane shear modulus of T300/914 by the Iosipescu and 45° off-axis tests. *Compos Sci Technol* 52(1):61–72